*minerals*

MDPI

*Article*

# Small-Scale Porphyry Cu (Au) Systems in Collisional Orogens: A Case Study of the Xifanping Deposit with Implications for Mineralization Potential in Western Yangtze Craton, SW China

**Yunhai Hu [1], Mimi Yang [2,3,*], Xingyuan Li [4], Guoxiang Chi [3] and Fufeng Zhao [5]**

[1] College of Human Settlements, Mianyang Normal University, Mianyang 621000, China
[2] College of Geography and Environment, Mianyang Normal University, Mianyang 621000, China
[3] Department of Geology, University of Regina, Regina, SK S4S 0A2, Canada
[4] College of Earth and Environmental Sciences, Lanzhou University, Lanzhou 730000, China
[5] College of Earth Science, Chengdu University of Technology, Chengdu 610059, China
* Correspondence: mmy2020@mtc.edu.cn

## Abstract

The Xifanping Cu–(Au) deposit, a small-scale porphyry system in the central Jinshajiang–Red River tectonic belt (JSRR), formed in a Cenozoic collisional setting. This study integrates zircon U–Pb geochronology, Lu–Hf isotopes, whole-rock geochemistry, and zircon trace element analyses of ore-bearing and barren porphyries, combined with regional comparisons, to constrain magma sources, metallogenic controls, and genetic processes. Ore-bearing biotite quartz monzonite porphyries were emplaced at 32.15 ± 0.43 Ma and 32.49 ± 0.57 Ma, post-dating barren quartz monzonite porphyry (33.15 ± 0.51 Ma). These ages are consistent with molybdenite Re–Os ages (32.1 ± 1.6 Ma), indicating near-synchronous magmatism and mineralization. Both porphyry types belong to the shoshonitic, peraluminous series, enriched in LILE, depleted in HFSE, enriched in LREE, and lacking significant Eu anomalies. Their εHf (t) values (–2.94 to +3.68) and crustal model ages (TDM2 = 0.88–1.30 Ga) indicate derivation from Neoproterozoic subduction-modified lower crust. Ore-bearing porphyries, however, exhibit higher zircon $Ce^{4+}/Ce^{3+}$ ratios (average = 584 vs. 228 for barren porphyries) and elevated hydrous mineral contents (>10 vol.% amphibole + biotite), indicating more oxidized and water-rich parental magmas. Compared with large-scale porphyry systems (e.g., Dexing, northern Chile), the absence of adakitic signatures and only moderate oxidation limited the scale of mineralization. Overall, the Xifanping deposit formed through partial melting of Neoproterozoic subduction-modified lower crust in a post-collisional extensional regime: at ~33.2 Ma, melting of metasomatized ancient lower crust generated barren porphyries; at ~32 Ma, further evolution and differentiation of this lower crust magmas led to the extraction and enrichment of ore-forming materials from the thicken lower crust, producing hydrated, oxidized, ore-bearing magmas that intruded at shallow levels to form base and precious metal mineralizations. These results underscore the distinctive metallogenic characteristics of small-scale porphyry systems in collisional settings and provide new insights into how source composition and magma oxidation state constrain mineralization potential.

**Keywords:** porphyry Cu-Au deposit; collisional setting; zircon $Ce^{4+}/Ce^{3+}$ ratio; Xifanping; Jinshajiang–Red River tectonic belt (JSRR)

check for updates

Academic Editor: Panagiotis Voudouris, Huanhuan Yang and Zhi Zhang

Received: 14 August 2025
Revised: 9 September 2025
Accepted: 17 September 2025
Published: 20 September 2025

**Citation:** Hu, Y.; Yang, M.; Li, X.; Chi, G.; Zhao, F. Small-Scale Porphyry Cu (Au) Systems in Collisional Orogens: A Case Study of the Xifanping Deposit with Implications for Mineralization Potential in Western Yangtze Craton, SW China. *Minerals* **2025**, *15*, 1001. https://doi.org/10.3390/min15091001

**Copyright:** © 2025 by the authors. Licensee MDPI, Basel, Switzerland. This article is an open access article distributed under the terms and conditions of the Creative Commons Attribution (CC BY) license (https://creativecommons.org/licenses/by/4.0/).

## 1. Introduction

Porphyry Cu (Mo–Au) deposits constitute the world's most important source of copper, typically forming in association with magmatic activity in subduction-related tectonic settings [1]. In contrast, their genesis in collisional settings—where active subduction is absent—remains a subject of longstanding debate, as exemplified by the Qinling and Dabie Mo belt in eastern-central China [2–4], the Oligocene–Miocene Gangdese porphyry Cu-Mo belt in southern Tibet [5–7], and the Eocene–Miocene Urumieh–Dokhtar Cu belt in central Iran [8,9]. In addition, the Sanjiang metallogenic belt in southeastern Tibet is among the most significant porphyry-producing regions, with substantial discoveries over the past decade. This Cenozoic porphyry Cu–Au polymetallic belt developed within a collisional–orogenic regime. The Jinshajiang–Red River tectonic belt (JSRR), a major structural corridor within the Sanjiang belt, traverses the Qiangtang Terrane and the western margin of the Yangtze Craton. It hosts a series of Cenozoic porphyry Cu–Au systems—including the Yulong Cu, Beiya Au–Cu, and Machangqing Cu–Mo–Au deposits—providing an exceptional natural laboratory for investigating porphyry mineralization in collisional settings [10]. The Xifanping Cu (Au) deposit, situated in the central segment of the JSRR, shares the same tectonic framework and similar mineralization age as several medium- to large-scale deposits in the region, yet is notably smaller in size (reserves: 0.18 Mt Cu at 0.28% Cu and 0.31 ppm Au [11]). Despite its limited scale, Xifanping remains a representative Cenozoic porphyry Cu (Au) system. While prior research on porphyry–skarn deposits in the belt has been extensive, it has overwhelmingly focused on larger deposits, overlooking the significance of small-scale systems, which can provide critical insights into mineralization processes at finer resolution [12]. This study addresses that gap by examining the Xifanping deposit to elucidate the link between magmatic evolution and porphyry mineralization in a collisional environment. The results aim to clarify the genetic mechanisms of small-scale porphyry Cu (Au) systems and contribute to a broader understanding of porphyry mineralization diversity under collisional tectonics.

This investigation integrates petrographic examination, zircon U–Pb geochronology, zircon trace element and Lu–Hf isotope analyses, and whole-rock geochemical characterization of ore-bearing and barren porphyries at Xifanping. It also incorporates published datasets on multiphase porphyry intrusions for comparative analysis. The study's specific objectives are to (1) establish the temporal and spatial relationship between magmatism and mineralization; (2) identify the magma sources for ore-bearing and barren intrusions; (3) compare lithological, geochemical, and mineralogical attributes of ore-bearing versus barren porphyries, with emphasis on the key controls on mineralization; and (4) reveal the genetic processes responsible for the Xifanping deposit within a collisional framework.

## 2. Geological Background

### *2.1. Regional Geology*

Geologically, the Xifanping Cu (Au) deposit lies within the central JSRR, a major metallogenic province in the Sanjiang orogen of southwestern China (Figure 1b) [10,13]. The belt straddles the Qiangtang Terrane and the western Yangtze Craton, forming part of the eastern segment of the India–Asia collision zone (Figure 1a) [14].

The lithosphere of the western Yangtze Craton was extensively reworked by Neoproterozoic subduction (ca. 1000–740 Ma) [15], producing plutonic and volcanic assemblages along the Panxi–Hannan arc [16] and thickening the lower crust [17,18]. In the late Permian (ca. 260–250 Ma), mantle plume activity generated the Emeishan Large Igneous Province (ELIP) along the craton's western margin. Following the closure of Paleo-Tethyan oceanic domains in the Late Triassic, this margin evolved into an intracontinental setting [19,20].

During the Cenozoic era, the India–Asia collision at ca. 55 Ma drove intense eastward extrusion across the Tibetan Plateau and adjacent regions, accommodated by major strike-slip faults such as the Jinshajiang–Red River, Gaoligong, Batang–Lijiang, and Jiali faults [21]. Between the Eocene and Oligocene (ca. 40–30 Ma), ongoing plate convergence led to convective removal of the lower lithospheric mantle, generating a ~1000 km-long belt of potassic igneous rocks along the cratonic margin (Figure 1b) [20,22]. Small stocks with outcrops ranging between 0.8 and 3 km$^2$ are exposed as potassic igneous rocks, consisting of mafic to felsic lithologies. Many of these potassic intrusions are closely associated, both temporally and spatially, with porphyry Cu–Mo–Au mineralization [23,24], such as the Yulong Cu, Beiya Au–Cu, Machangqing Cu–Mo–Au, Tongchang Cu–Mo, and Habo Cu–Au deposits (Figure 1b) [18].

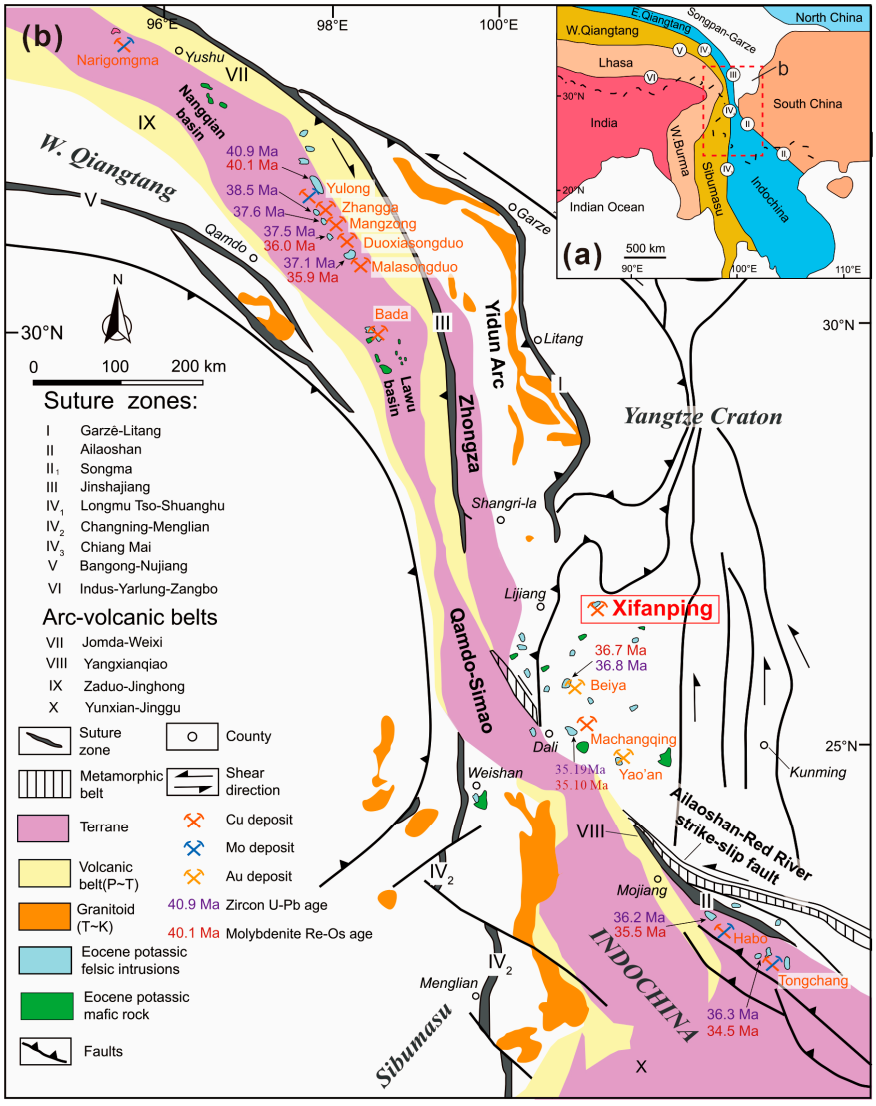


**Figure 1.** (**a**) Distribution of major continental blocks and sutures in the East Tethyan orogenic belt (modified from [25]). (**b**) Tectonic framework of the Sanjiang region, SW China (modified from [10,24]). Zircon U-Pb and molybdenite Re-Os ages for the porphyry–skarn ore belt are from [21].

## 2.2. Deposit Geology

The Xifanping deposit, located in Yanyuan County, Sichuan Province, lies on the southwestern margin of the Yangtze Platform within the Sanjiang Tethys orogenic belt (Figure 2a). It is situated approximately 100–150 km east of the Jinshajiang fault (Figure 1b).

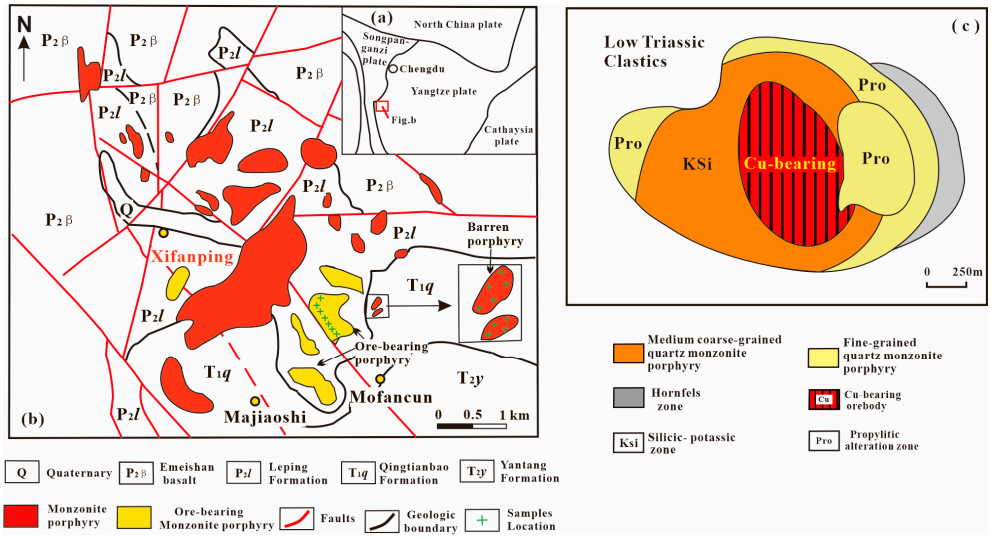


**Figure 2.** Geologic maps of the Xifanping deposit: (**a**) regional structural domains; (**b**) geologic sketch with sample locations (modified after [11]); (**c**) simplified map showing alteration zonation and mineralization (modified after [26]).

In the Xifanping mining area, the Upper Permian Leping Formation and Lower Triassic Qingtianbao Formation clastic rock sequences are exposed (Figure 2b). The district hosts hundreds of small porphyry intrusions, typically less than 0.5 km$^2$ in area, occurring as stocks and dikes. Quartz monzonite porphyry predominates, accompanied by minor vein-like quartz syenite porphyry, dioritic porphyrite, and lamprophyre dykes. The principal ore-forming phase is biotite quartz monzonite porphyry, which intrudes the Permo-Triassic clastic sequences and is associated with hornfels alteration. Copper–gold ore bodies occur both within and adjacent to the contact zone between the mineralized porphyry and surrounding rocks (Figure 2c).

Alteration within the Xifanping porphyry intrusions is intense and well-zoned. From the intrusion core outward, the alteration sequence comprises a deep potassic alteration zone, a shallower propylitic zone, and a peripheral hornfels zone (Figure 2c). Propylitic alteration, although comparatively weak, forms a broad halo in the wall rocks. This zoning is also evident in cross-section, consistent with alteration patterns typical of porphyry deposits.

The deposit contains reserves of 0.18 Mt Cu, grading 0.28% Cu and 0.31 ppm Au [11]. Mineralization is dominated by porphyry-type assemblages. Cu–Mo ore bodies consist mainly of veinlet- and disseminated pyrite–chalcopyrite–magnetite–native gold ± molybdenite ± galena ± sphalerite, hosted both within porphyry intrusions and along their contacts with clastic wall rocks. Early-stage mineralization is characterized by quartz veins and stockwork ore rich in molybdenite, associated with potassic alteration. Late-stage mineralization consists of veinlet- and disseminated-type ores containing only minor molybdenite, linked to propylitic alteration dominated by chlorite and calcite.

## 3. Sampling and Analytical Methods

### *3.1. Sampling*

Representative ore-bearing and barren monzonite porphyry samples were collected from both surface and subsurface locations (sampling sites shown in Figure 2b). Ore-bearing samples XFP1024 and XFP1026, and barren sample XFP1633, were selected for zircon LA–ICP–MS U–Pb dating, zircon trace element analysis, and Lu–Hf isotope analysis. Following petrographic examination, 15 relatively fresh monzonite porphyry samples (nine ore-bearing and six barren) were chosen for whole-rock geochemical analysis.

### *3.2. Analytical Methods*

Zircon grains from samples XFP1024, XFP1026, and XFP1633 were separated using standard magnetic and heavy liquid methods, followed by hand-picking under a binocular microscope. Sample preparation was conducted at the Langfang Regional Geological Survey Institute, Langfang City, Hebei Province, China. The LA–ICP–MS analyses were performed at Wuhan Sample Solution Analytical Technology Co., Ltd., Wuhan City, Hubei Province, China, using a 193 nm laser coupled to an Agilent 7500a ICP–MS (Agilent, Santa Clara, CA, USA). The operating parameters included 80 mJ laser energy and a 10 Hz repetition rate. Each analysis consisted of 20–30 s background acquisition (laser-off) followed by 50 s sample data acquisition (laser-on). The zircon standard 91500 was analyzed after every five unknowns as an external standard. U–Th–Pb concentrations were calibrated using $^{29}Si$ as an internal standard and NIST 610 glass as a reference material. Age calibration employed the Temora zircon standard ($^{206}Pb/^{238}U$ = 416.8 Ma [27]). Detailed analytical protocols follow [28,29]. Weighted mean ages and concordia plots were produced with ISOPLOT 3.0 [30], with uncertainties reported at the 1σ level (Table S1). Zircon Ce anomalies and $Ce^{4+}/Ce^{3+}$ ratios were calculated following the methods of [31–34].

The whole-rock elemental analyses were performed at the Beijing Research Institute of Uranium Geology. The samples were pulverized to 200 mesh. Major elements were quantified using a Philips PW 2404 X-ray fluorescence spectrometer (Almelo, The Netherlands) (Rh anode X-ray source) following [35], achieving analytical precision better than 1%. For trace element determinations, 25 mg of powdered material (including molybdenite and gold-bearing pyrite) was digested with HF + $HNO_3$ + $HClO_4$ in Savillex® Teflon vessels within high-pressure digestion bombs. Trace elements, including rare earth elements (REEs), were measured on a Finnigan-MAT Element-I ICP–MS following [36]. Analytical quality was monitored using geochemical reference materials GSR-3 and GSR-15, yielding precision better than 5%.

In situ Hf isotope ratios were analyzed at Wuhan Sample Solution Analytical Technology Co., Ltd. using laser ablation–multi-collector inductively coupled plasma–mass spectrometry (LA–MC–ICP–MS). The setup consisted of a Thermo Scientific™ Neptune Plus™ MC–ICP–MS (Dreieich, Germany) coupled with a GeoLas 2005 excimer laser ablation system (Lambda Physik, Goettingen, Germany). All the measurements were conducted in single-spot mode with a 44 μm crater diameter. Each analysis comprised 20 s of background signal acquisition (laser-off) followed by 50 s of ablation (laser-on). Detailed operating parameters are described in [37].

## 4. Results

### *4.1. Petrography*

The ore-bearing samples from the Xifanping deposit are mainly biotite quartz monzonite porphyries, whereas the barren samples are predominantly quartz monzonite porphyries. Representative hand specimens and photomicrographs are shown in Figure 3.

Ore-bearing biotite quartz monzonite porphyries occur in the northern, central, and western sectors of the mining area. They are grayish-white, with a porphyritic texture and massive structure (Figure 3c). Phenocrysts (0.6–2.5 cm) comprise plagioclase (30–35 vol.%), K-feldspar (30–35 vol.%), minor quartz (8–15 vol.%), biotite (8–10 vol.%), and amphibole (5–6 vol.%). Plagioclase rims exhibit sericitization, and K-feldspar shows minor alteration with perthitic texture. Biotite is pale brown (1–3 mm), and amphibole is dark green and has generally undergone intense alteration (Figure 3d). The groundmass is aphanitic to semi-cryptocrystalline, consisting mainly of feldspar, quartz, and biotite. Major accessory minerals include apatite, titanite, and zircon.

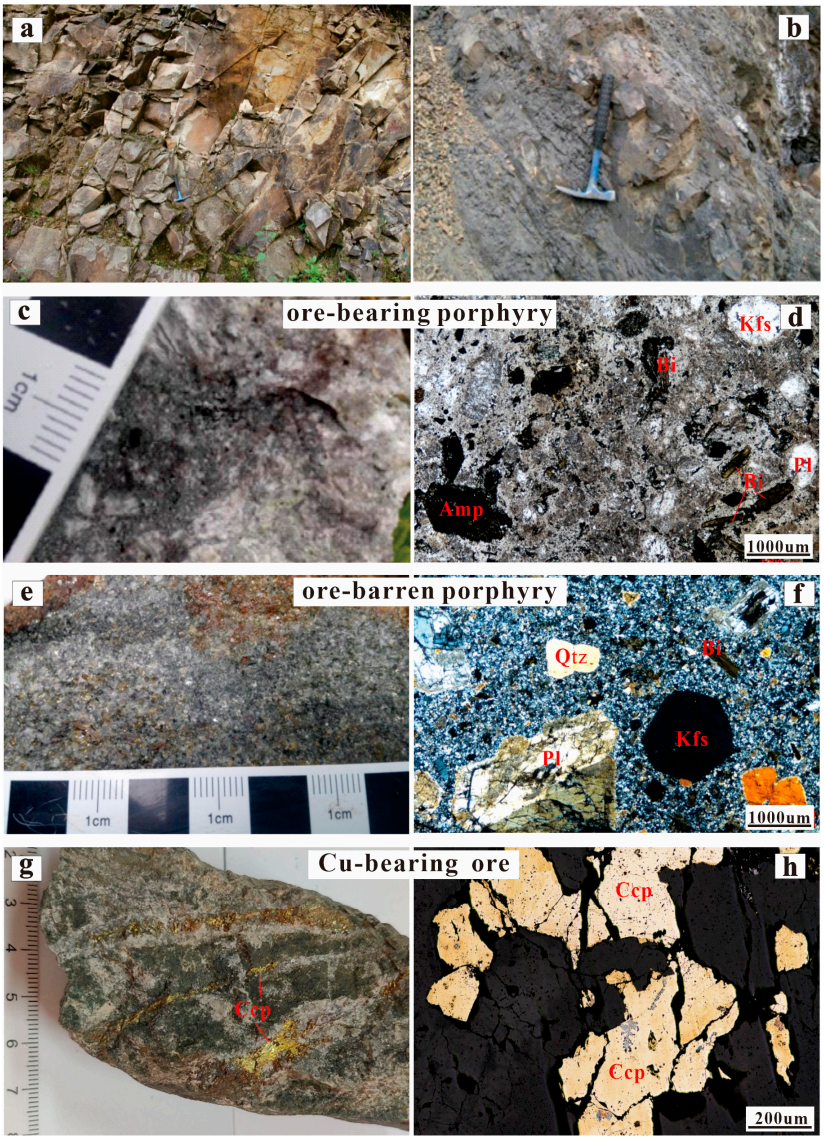


**Figure 3.** (**a**,**b**) Outcrop of monzonite porphyry intrusions; (**c**,**d**) ore bearing medium-grained biotite quartz monzonite porphyries samples ((**c**)—macroscopic photograph; (**d**)—transmitted light optical microscopy (crossed polars) photomicrograph); (**e**,**f**) Ore barren fine-grained quartz monzonite porphyries samples ((**e**)—macroscopic photograph; (**f**)—transmitted light optical microscopy (crossed polars) photomicrograph); (**g**,**h**) Veined copper-bearing ore ((**g**)—macroscopic photograph; (**h**)—reflected light optical microscopy (crossed polars) photomicrograph). Abbreviations: Pl: plagioclase; Kfs: potash feldspar; Otz: quartz; Amp: amphibole; Bi: biotite; Ccp: chalcopyrite.

Barren quartz monzonite porphyries are widespread but vary in outcrop size. They are yellowish-white, with porphyritic texture and massive structure (Figure 3e), and generally exhibit weak alteration. Phenocrysts (0.4–1.5 cm) include plagioclase (35–40 vol.%), K-feldspar (30–35 vol.%), quartz (15–20 vol.%), and biotite + amphibole (<5 vol.%) (Figure 3f). The groundmass is aphanitic to semi-cryptocrystalline, dominated by feldspar and quartz. Major accessory minerals are zircon and titanite.

Microscopic observations reveal three key differences: (1) the ore-bearing porphyries contain higher proportions of hydrous minerals (amphibole + biotite > 10 vol.%) than the barren porphyries, suggesting more water-rich magmas; (2) mineral grains in ore-bearing porphyries are significantly larger, indicating a higher degree of crystallization; and (3) alteration is markedly stronger in ore-bearing porphyries, implying a close link between alteration and mineralization.

### *4.2. Zircon U-Pb Geochronology*

Zircon U–Pb dating results for the monzonite porphyries at Xifanping are presented in Table S1 and Figure 4. Zircons from both the ore-bearing and barren porphyries are euhedral to subhedral prisms with gray-black color and distinct oscillatory zoning. Grain sizes range from 50 to 150 μm with aspect ratios of ~1:1.5 (Figure 4), and all have Th/U ratios >0.4.

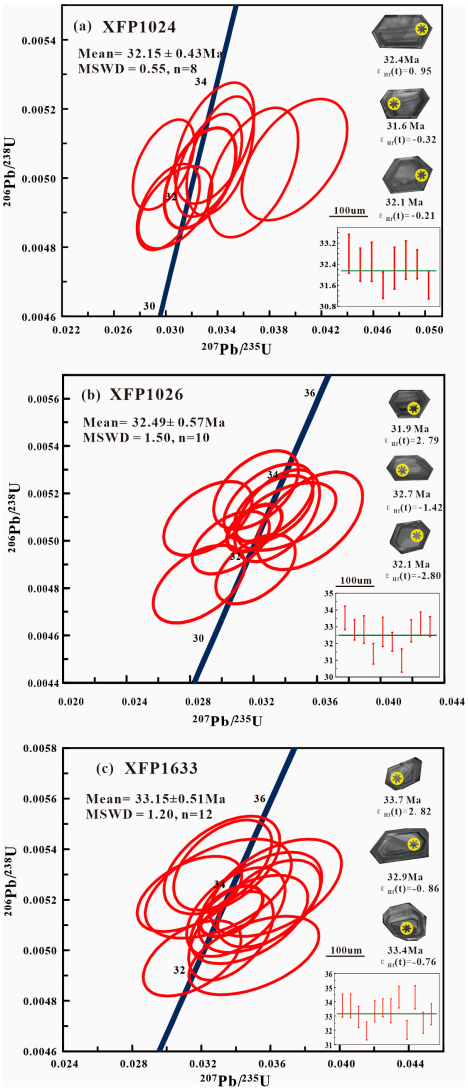


**Figure 4.** Representative zircon cathodoluminescence (CL) images and U–Pb concordia diagrams for the ore-bearing and barren porphyries from the Xifanping deposit. The yellow circles indicate laser ablation spots. Individual analytical uncertainties are reported at 1σ in data tables; concordia diagrams show 2σ error ellipses with weighted mean ages quoted at 95% confidence.

**Sample XFP1024 (ore-bearing):** Eight analytical spots yield $^{206}Pb/^{238}U$ ages of 31.61–32.80 Ma, with a weighted mean age of 32.15 ± 0.43 Ma (MSWD = 0.55) and Th/U ratios of 0.54–1.25.

**Sample XFP1026 (ore-bearing):** Ten analytical spots yield $^{206}Pb/^{238}U$ ages of 30.98–33.53 Ma, with a weighted mean age of 32.49 ± 0.57 Ma (MSWD = 1.50) and Th/U ratios of 0.83–1.32.

**Sample XFP1633 (barren):** Twelve analytical spots yield $^{206}Pb/^{238}U$ ages of 31.95–34.31 Ma, with a weighted mean of 33.15 ± 0.51 Ma (MSWD = 1.20) and Th/U ratios of 0.84–1.11.

These data indicate that both ore-bearing and barren porphyries were emplaced during the early Oligocene, with barren intrusions slightly earlier than the ore-bearing ones.

### *4.3. Whole-Rock Geochemistry*

The ore-bearing porphyries are characterized by high $SiO_2$ (62.67–68.81 wt.%, avg. 65.63 wt.%), $Al_2O_3$ (15.40–17.08 wt.%, avg. 16.37 wt.%), and $K_2O$ (4.38–6.28 wt.%, avg. 5.04 wt.%), with $K_2O/Na_2O$ ratios of 0.89–1.85 (avg. 1.09) and A/CNK values of 1.29–1.76 (avg. 1.49) (Figure 5; Table S2). They display elevated Sr/Y ratios (36.42–84.32, avg. 58.58) and low Y contents (14.50–29.90 ppm, avg. 18.96 ppm), along with low MgO (0.70–1.95 wt.%, avg. 1.24 wt.%), Mg# (31.64–45.90, avg. 37.97), Cr (12.70–71.70 ppm, avg. 29.16 ppm), and Ni (8.29–64.50 ppm, avg. 23.92 ppm) (Figure 6; Table S2). REE patterns show no significant Eu anomalies (Eu/Eu* = 0.62–0.89), wide-ranging total REE (ΣREE = 261–453 ppm, avg. 348 ppm), and pronounced LREE enrichment over HREE (Figure 7; Table S2).

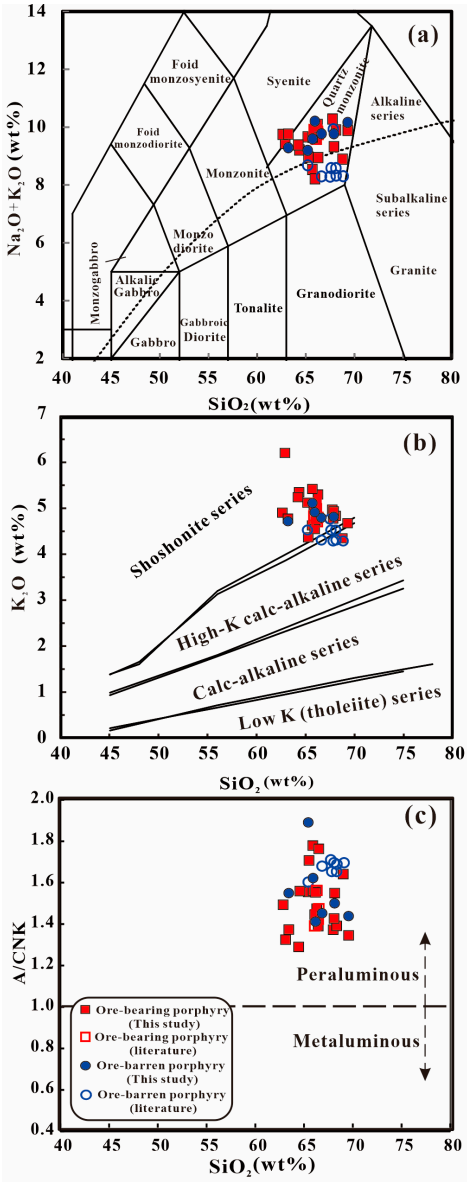


**Figure 5.** (**a**) TAS diagram [38]; (**b**) $K_2O$ vs. $SiO_2$ [39]; (**c**) A/CNK vs. $SiO_2$ [40] diagram. A/CNK = $Al_2O_3/(CaO + Na_2O + K_2O)$. Literature data are from [41].

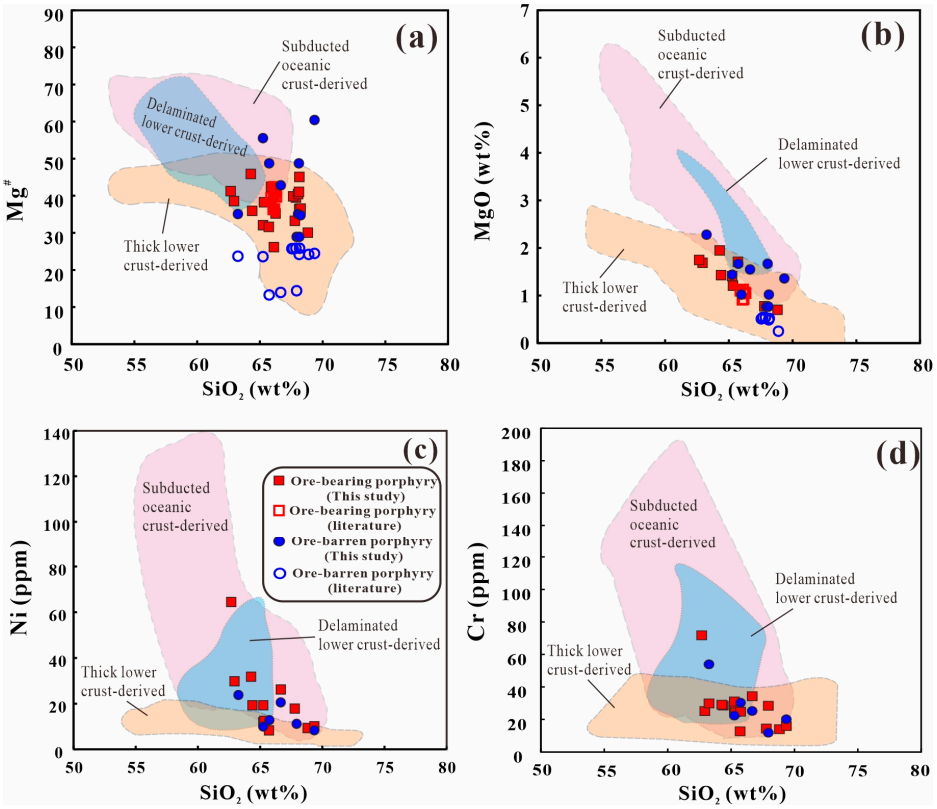


**Figure 6.** (**a**) Mg#, (**b**) MgO (wt.%), (**c**) Ni (ppm), and (**d**) Cr (ppm) vs. $SiO_2$ (wt.%) (modified after [42]).

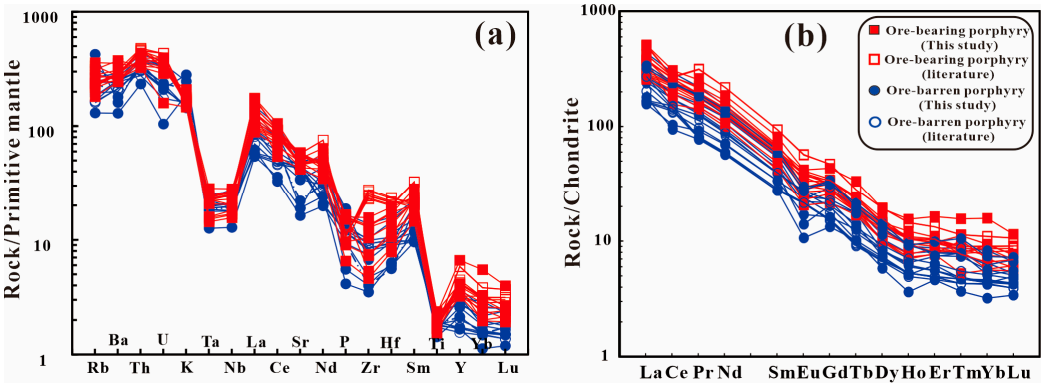


**Figure 7.** (**a**) Primitive mantle-normalized trace element diagrams; (**b**) chondrite-normalized rare earth element (REE) patterns for ore-bearing and barren porphyries. Normalization values from [43].

The barren porphyries exhibit similarly high $SiO_2$ (63.25–69.35 wt.%, avg. 67.20 wt.%), $Al_2O_3$ (15.42–17.99 wt.%, avg. 16.28 wt.%), and $K_2O$ (4.32–8.41 wt.%, avg. 5.19 wt.%), with $K_2O/Na_2O$ ratios of 0.93–4.08 (avg. 1.55) and A/CNK values of 1.44–1.89 (avg. 1.62) (Figure 5; Table S2). They show higher Sr/Y ratios (30.46–137.18, avg. 85.03) and lower Y contents (7.00–14.38 ppm, avg. 10.41 ppm) than the ore-bearing porphyries. MgO (0.25–2.28 wt.%, avg. 0.99 wt.%), Mg# (13.94–60.42, avg. 34.12), Cr (11.90–53.90 ppm, avg. 27.30 ppm), and Ni (8.36–23.80 ppm, avg. 14.46 ppm) are consistently low (Figure 6; Table S2). They also lack significant Eu anomalies (Eu/Eu* = 0.56–1.06) and show variable ΣREE (145–397 ppm, avg. 232 ppm) with LREE enrichment over HREE (Figure 7; Table S2).

Comparative geochemical analysis indicates (1) both ore-bearing and barren porphyries plot in the monzonite field on the TAS diagram (Figure 5a); (2) both belong to the shoshonitic series and are peraluminous (A/CNK > 1.1) (Figure 5b,c); (3) both exhibit

high Sr/Y ratios with low MgO, Cr, and Ni contents, but barren porphyries have higher Sr/Y (avg. 85.03 vs. 58.58) and lower MgO, Cr, and Ni (e.g., Ni: 14.46 vs. 23.92 ppm) (Figure 6a–d); (4) both are enriched in LILE (Rb, K, Ba) and depleted in HFSE (Nb, Ta, Zr) without significant Eu anomalies (Figure 7a,b); (5) both display wide ΣREE ranges with LREE enrichment, though ore-bearing porphyries have higher LREE contents and overall ΣREE (avg. 348 vs. 232 ppm); (6) the barren porphyry displays adakitic affinities, whereas the ore-bearing porphyry deviates from the adakitic field (Figure 8a,b).

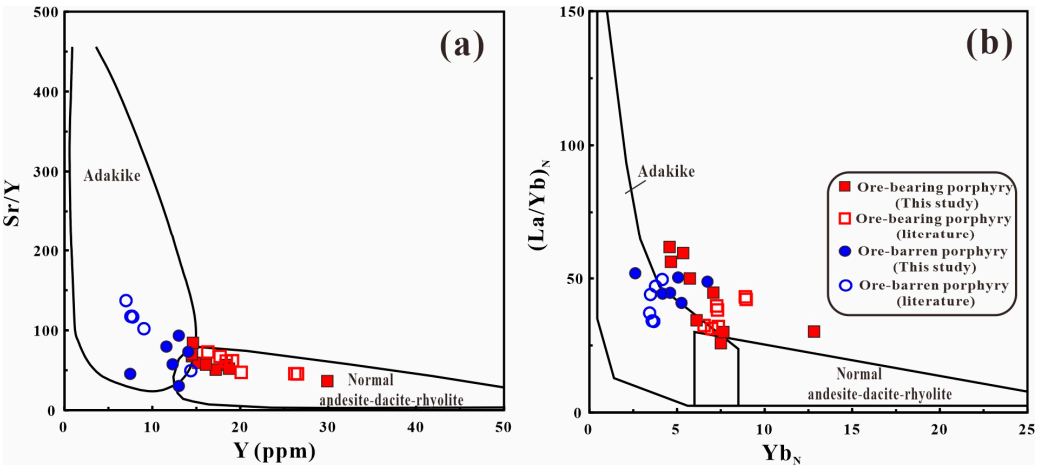


**Figure 8.** Plots of (**a**) Sr/Y vs. Y [44], and (**b**) La/Yb vs. Yb [45].

### *4.4. Zircon Lu–Hf Isotopes*

In situ zircon Hf isotopic analyses for monzonite porphyries at Xifanping (Table S3; Figure 9), corresponding to U–Pb dated zircons (Figure 4), yield the following: 26 analytical spots.

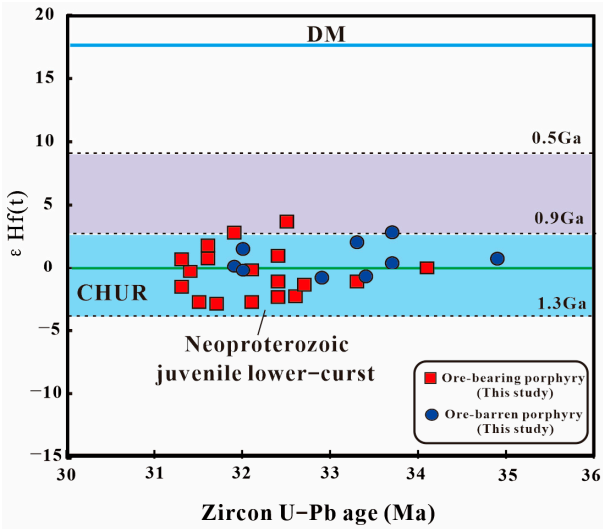


**Figure 9.** Zircon εHf (t) vs. U–Pb ages for Xifanping porphyries. The purple fields denote Neoproterozoic juvenile crustal growth episodes along the western Yangtze Craton margin [18]. Abbreviations: DM—Depleted Mantle; CHUR—Chondritic Uniform Reservoir.

**Sample XFP1024 (ore-bearing):** Initial $^{176}Hf/^{177}Hf$ = 0.282673–0.282802, εHf (t) = −2.80 to +1.77, TDM2 = 0.99–1.29 Ga.

**Sample XFP1026 (ore-bearing):** Initial $^{176}Hf/^{177}Hf$ = 0.282669–0.282856, εHf (t) = −2.94 to +3.68, TDM2 = 0.88–1.30 Ga

**Sample XFP1633 (barren):** Initial $^{176}Hf/^{177}Hf$ = 0.282727–0.282832, εHf (t) = −0.86 to +2.82, TDM2 = 0.93–1.17 Ga.

Ore-bearing and barren porphyries display overlapping εHf (t) ranges and similar TDM2 ages.

### *4.5. Magma Redox State*

Zircon trace element concentrations (Table S4) and chondrite-normalized REE patterns (Figure 10a) show:

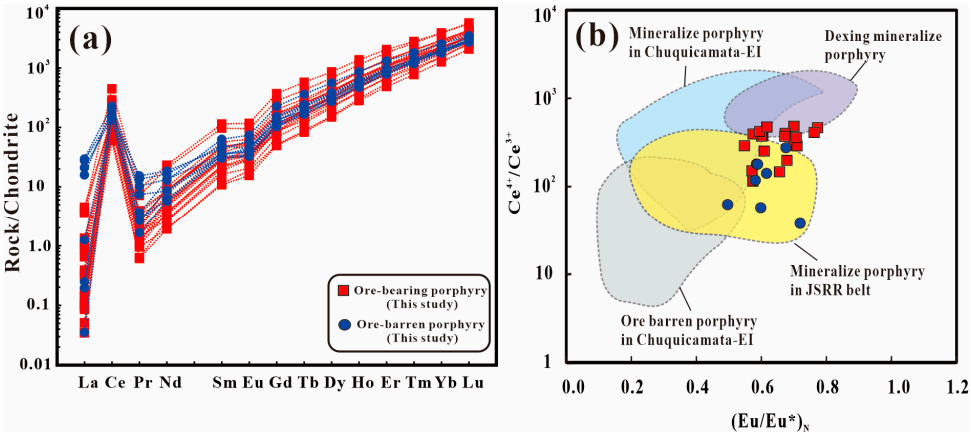


**Figure 10.** (**a**) Chondrite-normalized zircon REE patterns for ore-bearing and barren porphyries (normalization values from [43]). (**b**) Zircon $Ce^{4+}/Ce^{3+}$ vs. $(Eu/Eu^*)_N$ ratios. Comparison fields show compositional ranges for Chuquicamata-El Abra porphyry Cu belt (northern Chile) [31]; Dexing deposit [42]; Jinshajiang–Red River (JSRR) belt [46].

**Sample XFP1024 (ore-bearing):** Nine analytical spots yield $Ce^{4+}/Ce^{3+}$ = 255–814 (avg. 593), Eu/Eu* = 0.55–0.77 (avg. 0.65).

**Sample XFP1026 (ore-bearing):** Eleven analytical spots yield $Ce^{4+}/Ce^{3+}$ = 200–836 (avg. 575), Eu/Eu* = 0.57–0.71 (avg. 0.64).

**Sample XFP1633 (barren):** Eight analytical spots yield $Ce^{4+}/Ce^{3+}$ = 66–477 (avg. 228), Eu/Eu* = 0.50–0.72 (avg. 0.61).

Both ore-bearing and barren porphyries display typical magmatic zircon REE signatures, characterized by heavy REE (HREE) enrichment, positive Ce anomalies, and slight negative Eu anomalies. Notably, zircons from ore-bearing porphyries exhibit markedly higher $Ce^{4+}/Ce^{3+}$ ratios (200–836; avg. 584) compared with barren porphyries (66–477; avg. 228).

## 5. Discussion

### *5.1. Timing of Magmatism and Mineralization*

U–Pb geochronology from the Xifanping deposit constrains the emplacement of the ore-bearing porphyry to 32.15 ± 0.43 Ma and 32.49 ± 0.57 Ma, whereas the barren porphyry was emplaced at 33.15 ± 0.51 Ma (Figure 4). These results indicate that both porphyry types formed in the early Oligocene, with the ore-bearing phase slightly younger. Combined with the published Re–Os molybdenite age of 32.1 ± 1.6 Ma for the deposit [29], the data confirm that the major Cu–Au mineralization also occurred during the Oligocene. The data indicate a syngenetic origin to the porphyry sulfide ore, which is typical for porphyry-type deposits. Field evidence supports this interpretation, as Cu-bearing sulfides (e.g., chalcopyrite, molybdenite, and pyrite) and extensive alteration zones are predominantly hosted within or adjacent to ore-bearing intrusions (Figure 2c). Hence, the Xifanping deposit represents a significant porphyry mineralization event in the Sanjiang region of SW China.

In addition, the magmatism and mineralization at Xifanping (~32 Ma) postdate the main magmatic (~34–37 Ma) and mineralization (~34–36 Ma) peaks along the JSRR (Figure 1b) [11,21,38,39], and this age difference carries significant geological implications. From a regional geodynamic perspective, the delayed mineralization at Xifanping is likely attributed to the asthenospheric upwelling and crustal extension regime that still persists at ~32 Ma along the southeastern margin of the Tibetan Plateau. In terms of regional comparison, although Xifanping and other main-stage porphyry Cu deposits (such as Machangqing and Tongchang [47,48]) in the JSRR belong to the same collisional framework, the age difference in their formation indicates that the tectonic–magmatic–mineralization activity in the region did not end simultaneously but rather showed a characteristic of migration from northwest to southeast or the presence of locally sustained hotspots.

### *5.2. Sources of Ore-Bearing and Barren Magma*

The ore-bearing and barren monzonite porphyries both contain high $SiO_2$ contents (62.67–69.35 wt%), indicating they could not have been derived directly from mantle melting, as mantle-derived melts rarely exceed andesitic compositions ($SiO_2$ < 57 wt% [49]). Moreover, volcanic rocks in typical island arc settings—produced by partial melting of subducted slabs—commonly display $Na_2O$ enrichment ($K_2O/Na_2O$ < 0.5 [50]). In contrast, the Xifanping porphyries, formed in a collisional setting, are $K_2O$-rich ($K_2O/Na_2O$ = 0.89–4.08; mean = 1.32; Table S2), inconsistent with island arc affinities. Additionally, magmas derived from subducted slabs or delaminated mafic lower crust typically have elevated whole-rock Cr, Ni, and Mg# values, whereas the Xifanping porphyries show low Mg# (avg. 36.05), Cr (avg. 28.23 ppm), and Ni (avg. 19.19 ppm) (Figure 6; Table S2). These geochemical characteristics suggest the magmas were not sourced directly from slab melts or delaminated lower crust.

Instead, the whole-rock Mg#, MgO, Cr, and Ni contents overlap with those of igneous rocks derived from thickened lower crust (Figure 6). This interpretation is corroborated by zircon εHf (t) values, which yield crustal model ages (TDM2) of 0.88–1.30 Ga, consistent with the Neoproterozoic thickened/juvenile lower crust beneath the western Yangtze Craton (Figure 9) [17,18]. This crust, modified by subduction processes, is, therefore, the most likely source of the Xifanping porphyry magmas.

Comparative analysis shows that ore-bearing and barren porphyries share broadly similar major-, trace-, REE-element distributions and zircon Hf isotope range (Figures 5–7 and 9; Tables S2 and S3). However, the ore-bearing porphyry contains higher Y (avg. 18.96 ppm vs. 10.41 ppm), lower Sr/Y ratios (avg. 58.58 vs. 85.03), and lower MgO, Cr, and Ni contents (e.g., Ni avg. 14.46 ppm vs. 23.92 ppm) than the barren porphyry. On Sr/Y–Y and La/Yb–Yb diagrams (Figure 8), the barren porphyry displays adakitic affinities, whereas the ore-bearing porphyry deviates from the adakitic field. Collectively, both ore-bearing and barren porphyry types most probably have derived from the same, or similar, magma sources; however, they may have experienced different evolutionary and migration pathways.

### *5.3. Implications for the Porphyry Mineralization*

In the Xifanping deposit, ore-bearing and barren porphyries exhibit similar mineral assemblages; however, the ore-bearing porphyry contains abundant hydrous minerals—primarily amphibole and biotite (>10 vol.%) (Figure 3d)—which are markedly less common in barren counterparts. This mineralogical contrast indicates that the ore-bearing magma was substantially richer in water. Moreover, zircon from the ore-bearing porphyry displays significantly higher $Ce^{4+}/Ce^{3+}$ ratios (avg. 584) than that from the barren por-

phyry (avg. 228) (Table S4), reflecting a markedly higher oxidation state in the ore-bearing magma [51].

Comparisons of the Xifanping monzonite porphyries with other porphyry-type systems—including the Jiashajiang–RedRiver region (JSRR) and world-class deposits such as Dexing, China (~900 Mt Cu at 0.55% Cu [52]) and the Chuquicamata–El Abra Cu belt, northern Chile (840 Mt Cu at 0.82% Cu [31])—reveal that, according to Figure 10b, the Xifanping ore-bearing porphyry possesses a substantially higher oxidation state than barren Chilean intrusions, but slightly lower than mineralized intrusions in Chilean Cu belt and Dexing deposit, while being comparable to JSRR belt. In contrast, the barren porphyry at Xifanping exhibits oxidation states comparable to barren intrusions in Chile. These findings suggest that the relatively high oxidation state of the parental magma at Xifanping promoted Cu–Au migration and enrichment in hydrothermal fluids [1], yet the mineralization scale likely remains smaller than in globally significant systems such as Dexing or the Chilean Cu belt. By contrast, the barren porphyry parental magma was characterized by lower oxidation states and reduced water content, conditions less conducive to porphyry mineralization.

Studies of ore-bearing magmatic rocks in Cenozoic porphyry Cu deposits of northern Chile led Oyarzun et al. (2001, 2002) [53,54] to propose that typical calc-alkaline porphyries in continental and island-arc settings generally host only small-scale porphyry Cu deposits or remain barren, whereas large-scale deposits are associated with host rocks exhibiting adakitic geochemical signatures. Subsequent research has reinforced the genetic association between adakitic magmatism and porphyry–skarn Cu–Mo–Au mineralization [55–59]. The ore-bearing porphyry at Xifanping is petrogenetically distinct from adakites, and its parental magma has comparatively lower oxidation states than those of large-scale porphyry systems. These characteristics likely impose key constraints on the potential for giant Cu–Au mineralization and may explain the absence of large-scale porphyry Cu deposits discovered in the Xifanping district to date. Regarding Cenozoic porphyries in the southwestern margin of the Yangtze Craton, this study may provide crucial insights into why large-scale porphyry Cu deposits have neither been discovered nor reported in this region to date.

### *5.4. Genetic Mechanisms of Xifanping Deposit*

Although no oceanic crust subduction occurred during the early Oligocene, the Yangtze Craton lithospheric mantle had undergone multiple subduction-related metasomatic events. These include Neoproterozoic slab subduction (1000–740 Ma) [29] linked to the formation of the Panxi–Hannan arc [16], northward subduction of the Paleo-Tethyan oceanic slab (264–225 Ma) [60]. Oceanic slab subduction to asthenospheric depths induces dehydration and partial melting, and the Cu content of oceanic crust significantly exceeds that of continental crust [5]. In such settings, melts derived from subducted slabs and overlying sediments are enriched in water, sulfur, and Cu, and subsequently metasomatize the mantle wedge during ascent. This interaction promotes underplating at the crust–mantle boundary and the formation of thickened lower crust [61]. Thickened lower crust at craton margins can serve as a significant metal reservoir for porphyry deposits, as demonstrated by the Beiya Au–Cu deposit in the JSRR. The components within thickened crust further enhance the fertility of magmas [17]. Between 40 and 30 Ma, partial melting of these Neoproterozoic arc remnants likely contributed to the metal endowment for post-collisional porphyry systems in the region. Concurrently, during oceanic plate subduction, the ancient lower crust was likely modified by slab-derived fluids and mantle or mantle-wedge components [6], acquiring geochemical features conducive to crust–mantle interaction, such as the Lu–Hf isotopic signatures indicative of crust–mantle mixing.

During the Cenozoic era, after the collision of the Indian and Eurasian plates (~55 Ma), the magmatic activity at the Xifanping mining area should have undergone a continuous process. By the early Oligocene (~33.2 Ma), the corresponding geodynamic setting at the Xifanping was a post-collisional extensional regime [11,62]. Lithospheric decompression triggered partial melting of a predominantly Neoproterozoic ancient lower crustal source (Cu-poor, modified by slab-derived fluids), producing barren porphyries. Approximately one million years later (~32 Ma), further evolution and differentiation of these lower crust magmas led to the extraction and enrichment of ore-forming materials (water, sulfur, and Cu) from the thickened lower crust, producing Cu-bearing magmas emplaced at shallow crustal levels, ultimately forming the Cu-mineralized porphyry system at Xifanping.

## 6. Conclusions

(1) Timing of emplacement: Ore-bearing biotite quartz monzonite porphyries were emplaced at 32.15 ± 0.43 Ma and 32.49 ± 0.57 Ma, slightly later than the barren quartz monzonite porphyry (33.15 ± 0.51 Ma), indicating formation during the early Oligocene in a post-collisional extensional setting.

(2) Geochemical distinctions: Ore-bearing porphyries display higher zircon $Ce^{4+}/Ce^{3+}$ ratios, lower Sr/Y ratios, and greater hydrous mineral content (amphibole + biotite) than barren porphyries, reflecting more oxidized, water-rich parental magmas. However, the lack of adakitic signatures and a moderate oxidation state (relative to globally large-scale porphyry Cu–Au systems) constrained mineralization scale at Xifanping.

(3) Genetic model: At ~33.2 Ma, melting dominated by metasomatized ancient lower crust produced barren porphyries; at ~32 Ma, further evolution and differentiation of this lower crust magma led to the extraction and enrichment of ore-forming materials from the thickened lower crust, producing hydrated, oxidized, ore-bearing magmas that intruded at shallow levels to form mineralization.

**Supplementary Materials:** The following supporting information can be downloaded at: https://www.mdpi.com/article/10.3390/min15091001/s1. Table S1: LA–ICP–MS zircon U–Pb data of ore-bearing and barren porphyries from the Xifanping deposit; Table S2: Major(wt%) and trace (ppm) elemental test data of ore-bearing and barren porphyries from the Xifanping deposit; Table S3: In situ zircon Lu–Hf isotopes data of ore-bearing and barren porphyries from the Xifanping deposit; Table S4: Zircon trace element concentrations (ppm) of ore-bearing and barren porphyries from the Xifanping deposit.

**Author Contributions:** Y.H. and M.Y. conceived and designed the study; M.Y., Y.H., G.C., and X.L. participated in discussions; M.Y. and F.Z. conducted the field campaigns; M.Y. and Y.H. wrote the manuscript. All authors have read and agreed to the published version of the manuscript.

**Funding:** This work was supported by the Research Start-up Project of Mianyang Normal University (QD2021A13) and the Natural Science Foundation of Sichuan Province (2023NSFSC0792).

**Data Availability Statement:** Data available upon request from the corresponding authors.

**Acknowledgments:** We are grateful to the anonymous reviewers for their constructive suggestions, which greatly enhanced the quality of this research.

**Conflicts of Interest:** The authors declare no conflicts of interest.

## References

1. Richards, J.-P.; Spell, T.; Rameh, E.; Razique, A.; Fletcher, T. High Sr/Y magmas reflect arc maturity, high magmatic water content, and porphyry Cu ± Mo ± Au potential: Examples from the Tethyan arcs of central and eastern Iran and western Pakistan. *Econ. Geol.* **2012**, *107*, 295–332. [CrossRef]

2. Zheng, Y.; Ding, Z.; Cawood, A.; Yue, S. Geology, geochronology and isotopic geochemistry of the Xiaoliugou W-Mo ore field in the Qilian Orogen, NW China: Case study of a skarn system formed during continental collision. *Ore Geol. Rev.* **2017**, *81*, 575–586. [CrossRef]
3. Wang, T.; Wang, X.; Li, S.; Tong, Y.; Huang, H.; Zhang, L.; Zhang, J. Deep-crustal compositions and architecture from accretion to collision: Examples from the Central Asian Orogenic Belt and Qinling-Dabie orogen. *Acta Geol. Sin. (Engl. Ed.)* **2019**, *93*, 59–60. [CrossRef]
4. Zhang, F.; Wang, Y.; Dong, Y.; Cawood, A.; Fan, W. Early Cretaceous subductionmodified lithosphere beneath the eastern Qinling Orogen revealed from the Daying volcanic sequence in central China. *J. Asian Earth Sci.* **2019**, *176*, 209–228. [CrossRef]
5. Sun, X.; Lu, Y.-J.; McCuaig, T.-C.; Zheng, Y.-Y.; Chang, H.-F.; Guo, F.; Xu, L.-J. Miocene ultrapotassic, high-Mg dioritic, and adakite-like rocks from Zhunuo in Southern Tibet: Implications for mantle metasomatism and porphyry copper mineralization in collisional orogens. *J. Petrol.* **2018**, *59*, 341–386. [CrossRef]
6. Hou, Z.-Q.; Wang, R. Fingerprinting metal transfer from mantle. *Nat. Commun.* **2019**, *10*, 3510. [CrossRef]
7. Guo, L.; Zhang, H.-F.; Harris, N.; Luo, B.-J.; Zhang, W.; Xu, W.-C. Tectonic erosion and crustal relamination during the India-Asian continental collision: Insights from Eocene magmatism in the southeastern Gangdese belt. *Lithos* **2019**, *346–347*, 105161. [CrossRef]
8. Haschke, M.; Ahmadian, J.; Murata, M.; McDonald, I. Copper mineralization prevented by arc-root delamination during Alpine-Himalayan collision in central Iran. *Econ. Geol.* **2010**, *105*, 855–865. [CrossRef]
9. Holwell, D.-A.; Fiorentini, M.; McDonald, I.; Lu, Y.; Giuliani, A.; Smith, D.-J.; Keith, M.; Locmelis, M. A metasomatized lithospheric mantle control on the metallogenic signature of post-subduction magmatism. *Nat. Commun.* **2019**, *10*, 3511. [CrossRef]
10. Deng, J.; Wang, Q.-F.; Li, G.-J.; Santosh, M. Cenozoic tectono-magmatic and metallogenic processes in the Sanjiang region, southwestern China. *Earth-Sci. Rev.* **2014**, *138*, 268–299. [CrossRef]
11. Hou, Z.-Q.; Zeng, P.-S.; Gao, Y.-F.; Du, A.-D.; Fu, D.-M. Himalayan Cu–Mo–Au mineralization in the eastern Indo–Asian collision zone: Constraints from Re–Os dating of molybdenite. *Miner. Depos.* **2006**, *41*, 33–45. [CrossRef]
12. Cooke, D.-R.; Hollings, P.; Walshe, J.-L. Giant porphyry deposits: Characteristics, distribution, and tectonic controls. *Econ. Geol.* **2005**, *100*, 801–818. [CrossRef]
13. Hou, Z.-Q.; Zhang, H.-R.; Pan, X.-F.; Yang, Z.-M. Porphyry Cu (–Mo–Au) deposits related to melting of thickened mafic lower crust: Examples from the eastern Tethyan metallogenic domain. *Ore Geol. Rev.* **2011**, *39*, 21–45. [CrossRef]
14. Chung, S.-L.; Chu, M.-F.; Zhang, Y.-Q.; Xie, Y.-W.; Lo, C.-H.; Lee, T.-Y.; Lan, C.-Y.; Li, X.-H.; Zhang, Q.; Wang, Y.-Z. Tibetan tectonic evolution inferred from spatial and temporal variations in post-collisional magmatism. *Earth-Sci. Rev.* **2005**, *68*, 173–196. [CrossRef]
15. Sun, W.-H.; Zhou, M.-F.; Gao, J.-F.; Yang, Y.-H.; Zhao, X.-F.; Zhao, J.-H. Detrital zircon U-Pb geochronological and Lu-Hf isotopic constraints on the Precambrian magmatic and crustal evolution of the western Yangtze Block, SW China. *Precambrian Res.* **2009**, *172*, 99–126. [CrossRef]
16. Zhou, M.-F.; Ma, Y.-X.; Yan, D.-P.; Xia, X.-P.; Zhao, J.-H.; Sun, M. The Yanbian Terrane (Southern Sichuan Province, SW China): A Neoproterozoic arc assemblage in the western margin of the Yangtze Block. *Precambrian Res.* **2006**, *144*, 19–38. [CrossRef]
17. Hou, Z.-Q.; Zhou, Y.; Wang, R.; Zheng, Y.-C.; He, W.-Y.; Zhao, M.; Evans, N.-J.; Weinberg, R.-F. Recycling of metal–fertilized lower continental crust: Origin of non–arc Au–rich porphyry deposits at cratonic edges. *Geology* **2017**, *45*, 563–566. [CrossRef]
18. Zhou, Y.; Hou, Z.-Q.; Wang, R.; Zheng, Y.-C.; He, W.-Y.; Xu, B. Petrogenesis of Cenozoic high–Sr/Y shoshonites and associated mafic microgranular enclaves in an intracontinental setting: Implications for porphyry Cu-Au mineralization in western Yunnan, China. *Lithos* **2018**, *324–325*, 39–54. [CrossRef]
19. Wang, X.-F.; Metcalfe, I.; Jian, P.; He, L.-Q.; Wang, C.-S. The Jinshajiang- Ailaoshan Suture zone, China: Tectonostratigraphy, age and evolution. *J. Asian Earth Sci.* **2000**, *18*, 675–690. [CrossRef]
20. Lu, Y.-J.; McCuaig, T.-C.; Li, Z.-X.; Jourdan, F.; Hart, C.-J.-R.; Hou, Z.-Q.; Tang, S.-H. Paleogene post-collisional lamprophyres in western Yunnan, western Yangtze Craton: Mantle source and tectonic implications. *Lithos* **2015**, *233*, 139–161. [CrossRef]
21. Xu, L.-L.; Bi, X.-W.; Hu, R.-Z.; Zhang, X.-C.; Su, W.-C.; Qu, W.-J.; Hu, Z.-C.; Tang, Y.-Y. Relationships between porphyry Cu–Mo mineralization in the Jinshajiang–Red River metallogenic belt and tectonic activity: Constraints from zircon U–Pb and molybdenite Re–Os geochronology. *Ore Geol. Rev.* **2012**, *48*, 460–473. [CrossRef]
22. Lu, Y.-J.; Kerrich, R.; Kemp, A.-I.-S.; McCuaig, T.-C.; Hou, Z.-Q.; Hart, C.-J.-R.; Li, Z.-X.; Cawood, P.-A.; Bagas, L.; Yang, Z.-M.; et al. Intracontinental Eocene-Oligocene porphyry Cu mineral systems of Yunnan, Western Yangtze Craton, China: Compositional characteristics, sources, and implications for continental collision metallogeny. *Econ. Geol.* **2013**, *108*, 1541–1576. [CrossRef]
23. Wang, R.; Zhang, J.-B.; Luo, C.-H.; Zhou, Q.-S.; Xia, W.-J.; Zhao, Y. *Control of Deep Processes and Material Structure on Cu-REE Metallogenic System in Continental Collision Belt: A Case Study of Gangdise and Sanjiang Collision Belt*; Tongfang Knowledge Network (Beijing) Technology Co., Ltd.: Beijing, China, 2023; (In Chinese with English Abstract). [CrossRef]
24. He, W.-Y.; Mo, X.-X.; Yang, L.-Q.; Xing, Y.-L.; Dong, G.-C.; Yang, Z.; Gao, X.; Bao, X.-S. Origin of the Eocene porphyries and mafic microgranular enclaves from the Beiya porphyry Au polymetallic deposit, western Yunnan, China: Implications for magma mixing/mingling and mineralization. *Gondwana Res.* **2016**, *40*, 230–248. [CrossRef]

25. Metcalfe, I. Paleozoic and Mesozoic tectonic evolution and paleogeography of East Asian crustal fragments: The Korean Peninsula in context. *Gondwana Res.* **2006**, *9*, 24–46. [CrossRef]
26. Xu, S.-J.; Shen, W.-Z.; Wang, R.-C.; Lu, J.-J.; Lin, Y.-P.; Ni, P.; Luo, Y.-N.; Li, L.-Z. Characteristics and genesis of Xifanping porphyry copper deposit in Yanyuan, Sichuan Province. *Acta Mineral. Sin.* **1997**, *1*, 56–62.
27. Black, L.-P.; Kamo, S.-L.; Allen, C.-M.; Aleinikoff, J.-N.; Davis, D.-W.; Korsch, R.-J.; Foudoulis, C. TEMORA 1: A new zircon standard for Phanerozoic U-Pb geochronology. *Chem. Geol.* **2003**, *200*, 155–170. [CrossRef]
28. Liu, Y.-S.; Hu, Z.-C.; Gao, S.; Günther, D.; Xu, J.; Gao, C.-G.; Chen, H.-H. In situ analysis of major and trace elements of anhydrous minerals by LA-ICP-MS without applying an internal standard. *Chem. Geol.* **2008**, *257*, 34–43. [CrossRef]
29. Liu, Y.-S.; Gao, S.; Hu, Z.-C.; Gao, C.-G.; Zong, K.-Q.; Wang, D.-B. Continental and oceanic crust recycling-induced melt-peridotite interactions in the Trans-North China Orogen: U-Pb dating, Hf isotopes and trace elements in zircons of mantle xenoliths. *J. Petrol.* **2010**, *51*, 537–571. [CrossRef]
30. Ludwig, K.-R. *User's Manual for a Geochronology Toolkit for Microsoft Excel*; Berkeley Geochronology Center: Berkeley, CA, USA, 2003.
31. Ballard, J.-R.; Palin, M.-J.; Campbell, I.-H. Relative oxidation states of magmas inferred from Ce (IV)/Ce (III) in zircon: Application to porphyry copper deposits of northern Chile. *Contrib. Mineral. Petrol.* **2002**, *144*, 347–364. [CrossRef]
32. Ferry, J.-M.; Watson, E.-B. New thermodynamic models and revised calibrations for the Ti-in-zircon and Zr-in-rutile thermometers. *Contrib. Mineral. Petrol.* **2007**, *154*, 429–437. [CrossRef]
33. Trail, D.; Watson, E.-B.; Tailby, N.-D. The oxidation state of Hadean magmas and implications for early Earth's atmosphere. *Nature* **2011**, *480*, 79–82. [CrossRef]
34. Trail, D.; Watson, E.-B.; Tailby, N.-D. Ce and Eu anomalies in zircon as proxies for the oxidation state of magmas. *Geochim. Cosmochim. Acta* **2012**, *97*, 70–87. [CrossRef]
35. Gao, J.-F.; Lu, J.-J.; Lin, Y.-P.; Pu, W. Analysis of trace elements in rock samples using HR-ICPMS. *J. Nanjing Univ. (Nat. Sci.)* **2003**, *39*, 844–850, (In Chinese with English Abstract).
36. Qi, L.; Hu, J.; Gregoire, D.-C. Determination of trace elements in granites by inductively coupled plasma mass spectrometry. *Talanta* **2000**, *51*, 507–513. [CrossRef]
37. Hu, Z.; Liu, Y.; Gao, S.; Liu, W.; Zhang, W.; Tong, X.; Lin, L.; Zong, K.; Li, M.; Chen, H.; et al. Improved in situ Hf isotope ratio analysis of zircon using newly designed X skimmer cone and jet sample cone in combination with the addition of nitrogen by laser ablation multiple collector ICP-MS. *J. Anal. At. Spectrom.* **2012**, *27*, 1391–1399. [CrossRef]
38. Middlemost, E.-A.-K. Naming Materials in the Magma/igneous Rock System. *Earth Sci. Rev.* **1994**, *37*, 215–224. [CrossRef]
39. Collins, W.-J.; Scams, S.-D.; White, A.-J.-R. Nature and Origin of A–Type Uranitcs with Particular Reference to Southeastern Australia. *Contrib. Mineral. Petrol.* **1982**, *80*, 189–200. [CrossRef]
40. Maniar, P.-D.; Piccole, I.-P.-M. Tectonic Discrimination of Granitoids. *Geol. Soc. Am.* **1989**, *101*, 635–643. [CrossRef]
41. Huang, J.-H. Comparative Study on the Petrogenesis of the Ore-Bearing and Barren Porphyries from the Xifanping Copper Deposit in Yanyuan. Master's Thesis, China University of Geosciences, Beijing, China, 2019. (In Chinese with English Abstract).
42. Wang, Q.; Xu, J.-F.; Jian, P.; Bao, Z.-W.; Zhao, Z.-H.; Li, C.-F.; Xiong, X.-L.; Ma, J.-L. Petrogenesis of adakitic porphyries in an extensional tectonic setting, Dexing, South China: Implications for the genesis of porphyry copper mineralization. *J. Petrol.* **2006**, *47*, 119–144. [CrossRef]
43. Sun, S.-S.; McDonough, W.-F. Chemical and isotopic systematics of oceanic basalts, implications for mantle composition and processes. In *Magmatism in the Ocean Basin*; Geological Society Special Publication: London, UK, 1989; Volume 42, pp. 313–345.
44. Defant, M.-J.; Drummond, M.-S. Derivation of some morden arc magmas by of young subducted lithosphere. *Nature* **1990**, *347*, 662–665. [CrossRef]
45. Drummond, M.-S.; Defant, M.-J. A Model for Trondhjemite-tonalite-dacite Genesis and Crustal Growth Via Slab Melting: Archean to Modern Comparisons. *J. Geophys. Res.* **1990**, *95*, 21503–21521. [CrossRef]
46. Yang, Z.; Yang, L.-Q.; He, W.-Y.; Gao, X.; Liu, X.-D.; Bao, X.-S.; Lu, Y.-G. Control of magmatic oxidation state in intracontinental porphyry mineralization: A case from Cu (Mo–Au) deposits in the Jinshajiang-Red River metallogenic belt, SW China. *Ore Geol. Rev.* **2017**, *90*, 827–846. [CrossRef]
47. Yang, M.-M.; Zhao, F.-F.; Liu, X.-F.; Qing, H.-R.; Chi, G.-X.; Li, X.-Y.; Lai, C.-K. Contribution of magma mixing to the formation of porphyry-skarn mineralization in a post-collisional setting: The Machangqing Cu-Mo-(Au) deposit, Sanjiang tectonic belt, SW China. *Ore Geol. Rev.* **2020**, *122*, 103518. [CrossRef]
48. Yang, M.-M.; Zhao, F.-F.; Liu, X.-F.; Qing, H.-R.; Raharimahefa, T.; Duan, W.-J. Petrogenesis and geodynamic setting of granitoids at Machangqing Cu–Mo (Au) deposit, western Yangtze craton, southwestern China: Constraints from zircon U–Pb and molybdenite Re–Os geochronology, Lu–Hf isotopes, and geochemistry. *Can. J. Earth Sci.* **2020**, *57*, 1066–1088. [CrossRef]
49. Baker, E.-T.; Massoth, G.-J.; Feely, R.-A.; Embley, R.W.; Thomson, R.E.; Burd, B.J. Hydrothermal event plumes from the CoAxial seafloor eruption site, Juan de Fuca Ridge. *Geophys. Res. Lett.* **1995**, *22*, 147–150. [CrossRef]

50. Shu, Q.; Chang, Z.; Lai, Y.; Hu, X.; Wu, H.; Zhang, Y.; Wang, P.; Zhai, D.; Zhang, C. Zircon trace elements and magma fertility: Insights from porphyry (-skarn) Mo deposits in NE China. *Miner. Depos.* **2019**, *54*, 645–656. [CrossRef]
51. Shu, Q.; Deng, J. The composition of magmatic-hydrothermal fluids and their related metal mineralization. *Sci. China Earth Sci.* **2025**, *68*, 208–225. [CrossRef]
52. Zhang, H.; Ling, M.-X.; Liu, Y.-L.; Tu, X.-L.; Wang, F.-Y.; Li, C.-Y.; Liang, H.-Y.; Yang, X.-Y.; Arndt, N.-T.; Sun, W.-D. High oxygen fugacity and slab melting linked to Cu mineralization: Evidence from Dexing porphyry copper deposits, southeastern China. *J. Geol.* **2013**, *121*, 289–305. [CrossRef]
53. Oyarzun, R.; Marquez, A.; Lillo, J.; López, I.; Rivera, S. Giant versus small porphyry copper deposits of Cenozoic age in northern Chile: Adakitic versus normal calc-alkaline magmatism. *Miner. Depos.* **2001**, *36*, 794–798. [CrossRef]
54. Oyarzun, R.; Marquez, A.; Lillo, J.; López, I.; Rivera, S. Reply to discussion on "Giant versus small porphyry copper deposits of Cenozoic age in northern Chile: Adakitic versus normal calc-alkaline magmatism" by Oyarzun R, Márquez A, Lillo J, López I, Rivera S (Mineralium Deposita 36: 794–798, 2001). *Miner. Depos.* **2002**, *37*, 795–799. [CrossRef]
55. Mungall, J.-E. Roasting the mantle: Slab melting and the genesis of major Au and Au-rich Cu deposits. *Geology* **2002**, *30*, 915–918. [CrossRef]
56. Reich, M.; Parada, M.A.; Palacios, C.; Dietrich, A.; Schultz, F.; Lehmann, B. Adakite-like signature of Late Miocene intrusions at the Los Pelambres giant porphyry copper deposit in the Andes of central Chile: Metallogenic implications. *Miner. Depos.* **2003**, *38*, 876–885. [CrossRef]
57. Jiang, Y.-H.; Jiang, S.-Y.; Dai, B.-Z.; Liao, S.-Y.; Zhao, K.-D.; Ling, H.-F. Middle to Late Jurassic felsic and mafic magmatism in southern Hunan Province, Southeast China: Implications for a continental arc to rifting. *Lithos* **2009**, *107*, 185–204. [CrossRef]
58. Chiaradia, M.; Vallance, J.; Fontboté, L.; Stein, H.; Schaltegger, U.; Coder, J.; Richards, J.; Villeneuve, M.; Gendall, I. U-Pb, Re-Os, and $^{40}Ar/^{39}Ar$ geochronology of the Nambija Au-skarn and Pangui porphyry Cu deposits, Ecuador: Implications for the Jurassic metallogenic belt of the Northern Andes. *Miner. Depos.* **2009**, *44*, 371–387. [CrossRef]
59. Shu, Q.; Deng, J.; Chang, Z.; Wang, Q.; Niu, X.; Xing, K.; Sun, X.; Zhang, Z.; Zeng, Q.; Zhao, H.; et al. Skarn zonation of the giant Jiama Cu-Mo-Au deposit in southern Tibet, SW China. *Econ. Geol.* **2024**, *119*, 1–22. [CrossRef]
60. Zou, F.-H.; Wu, C.-L.; Gao, D.; Deng, L.-H.; Gao, Y.-H. Triassic granites in theWest Qinling Orogen, China: Implications for the Early Mesozoic tectonic evolution of the Paleo-Tethys ocean. *Int. Geol. Rev.* **2022**, *65*, 1923–1955. [CrossRef]
61. Hou, Z.; Wang, R.; Zhang, H.; Zheng, Y.; Jin, S.; Thybo, H.; Weinberg, R.F.; Xu, B.; Yang, Z.; Hao, A.-W.; et al. Formation of giant copper deposits in Tibet driven by tearing of the subducted Indian plate. *Earth-Sci. Rev.* **2023**, *243*, 104482. [CrossRef]
62. Yang, M.; Li, X.; Chi, G.; Song, H.; Xu, Z.; Zhao, F. Petrogenesis and Geodynamic Mechanisms of Porphyry Copper Deposits in a Collisional Setting: A Case from an Oligocene Porphyry Cu (Au) Deposit in Western Yangtze Craton, SW China. *Minerals* **2024**, *14*, 874. [CrossRef]


**Disclaimer/Publisher's Note:** The statements, opinions and data contained in all publications are solely those of the individual author(s) and contributor(s) and not of MDPI and/or the editor(s). MDPI and/or the editor(s) disclaim responsibility for any injury to people or property resulting from any ideas, methods, instructions or products referred to in the content.